# Amorphous antimony oxide as reaction pathway modulator toward electrocatalytic glycerol oxidation for selective dihydroxyacetone production

Dongkyu Kim [a,b,1], Won-Gwang Lim [c,1,2], Youngmin Kim [a], Lee Seul Oh [a,b], Seongseop Kim [d], Jong Hyeok Park [b], Changshin Jo [e], Hyung Ju Kim [a], Joonhee Kang [f,*], Seonggyu Lee [g,h,*], Eunho Lim [a,*]

[a] Chemical & Process Research Division, Korea Research Institute of Chemical Technology (KRICT), 141 Gajeongro, Daejeon 34114, Republic of Korea
[b] Department of Chemical and Biomolecular Engineering, Yonsei University, 50 Yonseiro, Seoul 03722, Republic of Korea
[c] Department of Chemical and Biomolecular Engineering, Korea Advanced Institute of Science and Technology (KAIST), 291 Daehak-Ro, Yuseong-Gu, Daejeon 34141, Republic of Korea
[d] School of Chemical Engineering, Clean Energy Research Center, Jeonbuk National University, 567 Baekje-daero, Jeonju 54896, Republic of Korea
[e] Graduate Institute of Ferrous & Energy Materials Technology (GIFT) and Department of Chemical Engineering, Pohang University of Science and Technology (POSTECH), Pohang 37637, Republic of Korea
[f] Department of Nanoenergy Engineering, Pusan National University (PNU), 2 Busandaehak-ro 63 beon-gil, Busan, Republic of Korea
[g] Department of Chemical Engineering, Kumoh National Institute of Technology (KIT), 61 Daehak-ro, Gumi 39177, Gyeongbuk, Republic of Korea
[h] Department of Energy Engineering Convergence, Kumoh National Institute of Technology (KIT), 61 Daehak-ro, Gumi 39177, Gyeongbuk, Republic of Korea

## A B S T R A C T

Achievement of an efficient and stable electrocatalytic glycerol oxidation reaction (EGOR) is limited by a lack of strategies for designing advanced electrocatalysts that satisfy the desired product selectivity, high electrocatalytic activity, and stability. Here, we report that the reaction pathway of EGOR can be modulated by the incorporation of amorphous antimony oxide ($SbO_x$) on the surface of a Pt nanoparticle electrocatalyst ($SbO_x$-Pt), which creates highly selective glycerol oxidation to dihydroxyacetone (DHA), one of the most valuable products of EGOR. The selective control of adsorption behaviors of glycerol oxidation products allows for $SbO_x$ to act as a reaction pathway modulator. Moreover, $SbO_x$ deposition on a Pt surface also enhances the stability, electrocatalytic activity, and glycerol conversion of the Pt electrocatalyst, and thus promotes the EGOR. As a result, the $SbO_x$-Pt electrocatalyst achieves a high DHA selectivity of 81.1%, which is about 11 times higher than that of commercial Pt/C electrocatalysts.

## 1. Introduction

As the production amount of biodiesel sharply increases, the annual production amount of glycerol, which is a major by-product of the biodiesel production process, reached three million tons in 2020 [1,2]. However, the demand for glycerol in industrial applications is low, so glycerol has been considered a low-value material [3]. The glycerol oxidation reaction, including thermo-catalytic oxidation [3,4] and bio-catalytic oxidation [5] has attracted attention because glycerol can

be converted to a variety of high value-added chemical products [6,7]. Among the methods for oxidizing glycerol, the electrocatalytic glycerol oxidation reaction (EGOR) is the most promising owing to its high energy efficiency and mild reaction conditions (*i.e.*, normal temperature and pressure without a need to use toxic oxidizing agents) [8,9]. In cathode part, hydrogen evolution reaction (HER, $2H^+ + 2e^- \rightarrow H_2$) occurs, whereas glycerol oxidation reaction ($C_3H_8O_3 \rightarrow C_3H_6O_3 + 2H^+ + 2e^-$) occurs in anode part [10–12]. This EGOR in anode has much lower oxidation potential than oxygen evolution reaction (OER), so it is

promising system to decrease the total amount of energy consumption (Fig. S1). Moreover, another reduction reaction (*e.g.,* $CO_2$ reduction reaction) can be also applied to produce valuable products at the cathode [13–15]. In anode part, various high value-added chemicals including glyceric acid (GLA), glyceraldehyde (GAD), dihydroxyacetone (DHA), and glycolic acid (GCA) can be produced by regulating the potential, electrolyte, and electrocatalysts [11,16–18]. DHA is the most valuable chemicals among the products of EGOR owing to its high cost ($150 per kg, 600 times more expensive than glycerol) [19]. Therefore, achieving high DHA selectivity in EGOR is critical.

To produce DHA as a main product in EGOR, multimodal approaches have been attempted to design electrocatalysts with high DHA selectivity. However, most of the previously reported electrocatalysts produce GLA and GCA as main products of EGOR which have lower value than DHA [20,21]. Even though several electrocatalysts including co-catalyst (*e.g.,* Ru and Bi) with a Pt electrocatalyst have been previously reported to selectively produce the DHA from EGOR, the number of electrocatalyst candidates which can produce mainly DHA is still deficient. Most importantly, previously reported electrocatalysts exhibited unsatisfactory DHA selectivity of only 50–70% [22–24]. In addition to the limitations to achieving high DHA selectivity in EGOR, poor reaction kinetics and stability in acidic conditions is considered another problem that needs to be addressed for efficient EGOR. In general, DHA easily undergoes interconversion to GAD in an alkaline electrolyte, followed by base-catalyzed oxidation to hydroxypyruvic acid (HPA) and tartronic acid (TTA) [25–27]. Therefore, the use of an acidic electrolyte is inevitable to accomplish the EGOR with high DHA selectivity. However, the kinetics and stability of EGOR in acidic conditions is relatively lower than those in alkaline conditions, so most of precedent researches performed EGOR in alkaline condition, resulting in low DHA selectivity [28]. Thus, there is a strong need to develop a strategy for designing advanced electrocatalysts that simultaneously satisfy the high DHA selectivity, promoted electrocatalytic activity, and outstanding stability in acidic conditions.

In this study, we designed advanced electrocatalysts to achieve high DHA selectivity, specific activity, mass activity, and stability in the EGOR in acidic conditions. We developed amorphous antimony oxide ($SbO_x$) incorporated on the surface of Pt nanoparticle electrocatalysts which are supported by ordered mesoporous carbon (OMC) supports (Fig. 1a and S2). The cylindrical porous carbon with large mesopores and high surface area facilitates the transfer of active species and inhibits the aggregation of electrocatalysts during EGOR. Most importantly, the incorporation of amorphous $SbO_x$ effectively modulates the EGOR reaction pathway by regulating the adsorption configuration and the strength of the reaction intermediates on the electrocatalyst surface (Fig. 1b). Further, the amorphous $SbO_x$ incorporation inhibits the interconversion reaction of DHA to other products, which maximizes the DHA selectivity because amorphous $SbO_x$ makes it possible to selectively increase the DHA adsorption strength on the electrocatalyst surface by forming an ionic bond between Sb atoms of amorphous $SbO_x$ and O atoms of DHA. It switches the glycerol oxidation pathway to direct formation of DHA, leading to the significantly high DHA selectivity (81.1%) which is about 11 times higher than that of Pt/C. Moreover, incorporation of amorphous $SbO_x$ on the Pt surface improves the electrocatalytic activity and stability of the Pt electrocatalysts in acidic conditions, resulting in high glycerol conversion and reaction rate.

## 2. Experimental

### 2.1. Materials

Tetraethyl orthosilicate (TEOS), Pluronic F127, hydrochloric acid solution (HCl, concentration of 35–37%), chloroplatinic acid hexahydrate ($\geq$ 37.50%), acetone (99.9%), and antimony chloride ($\geq$ 99.95%) were purchased from Sigma-Aldrich. Anhydrous ethyl alcohol (EtOH), 2-propanol (IPA, 99.5%), 0.5 M sulfuric acid ($H_2SO_4$) solution, 0.005 M $H_2SO_4$ solution, and hydrofluoric acid (HF, concentration of 49%) were purchased from Samchun Chemical. 1.0 M KCl was purchased from Daejung Chemicals & Materials. Nafion® solution (5 wt%, D521) was purchased from Dupont and glycerol ($\geq$ 95.0%) was

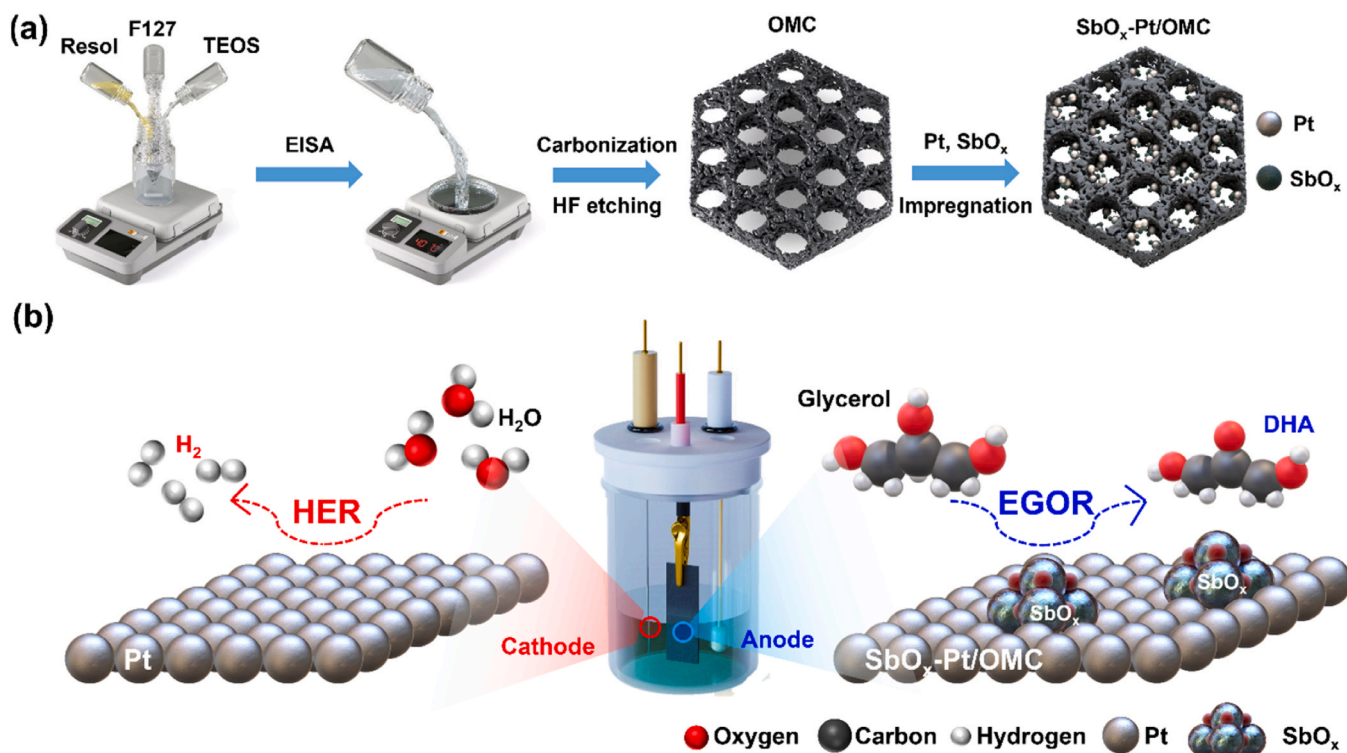

**Fig. 1.** (a) Schematic presentation for the synthesis of OMC and $SbO_x$-Pt/OMC electrocatalysts and (b) the effect of incorporation of amorphous $SbO_x$ on a Pt surface for modulating the EGOR pathway to achieve high DHA selectivity.

purchased from Junsei Chemical. Resol was synthesized *via* an amphiphilic surfactant templating method [29] and used as a carbon precursor. Commercial Pt/C (20 wt%), which was used as a control group, was purchased from Premetek.

## 2.2. Synthesis of OMC

OMC was synthesized by an evaporation-induced self-assembly (EISA) method [30] using TEOS and F127 as a silica precursor and a structure directing agent, respectively. First, 1.88 g of resol was dissolved in 9.38 mL of EtOH to prepare a homogeneous resol solution. 4.18 mL of TEOS was added to the resol solution. Second, 3.00 g of F127 was dissolved in 18.76 mL of EtOH to prepare the homogeneous F127 solution. Then, 1.88 mL of 0.2 M HCl was added to the F127 solution drop wise and stirred for 1 h at 45 ℃. Third, the resol solution was added to the F127 solution and stirred for 2 h to induce a sol-gel reaction. Then the solution was poured into a petri dish and the temperature of the hot plate was fixed to 40 ℃ to slowly evaporate the solvent. After removal of the solvent at 40 ℃, the petri dish was further annealed at 100 ℃ overnight. The as-made sample was heat-treated at 900 ℃ for 2 h under an argon gas flow to complete the preparation of the ordered mesoporous carbon silica (OMCS) composite. The OMCS was etched using a solution of HF, EtOH, and DI-water to completely remove the silica. After washing several times with DI-water, the OMC was dried in a vacuum oven overnight. Schematics of the OMC synthetic process is described in Fig. 1a and S2.

## 2.3. Synthesis of Pt/OMC and SbO_x-Pt/OMC electrocatalysts

The Pt/OMC electrocatalyst was synthesized by a wet impregnation method. For synthesis of Pt/OMC, 0.33 g of chloroplatinic acid hexahydrate was dissolved in 1.5 mL of anhydrous acetone. This solution was dropped onto 0.5 g of OMC powder and impregnated by grinding in a mortar. The mixture of the OMC and Pt precursor was dried in a vacuum oven at 60 ℃ overnight. Then, the dried powder was heat-treated at 200 ℃ for 2 h under a $H_2$ gas flow and cooled down to room temperature under a $N_2$ gas flow. The targeted Pt amount of Pt/OMC electrocatalyst was 20 wt%. The amounts of $SbO_x$ in the $SbO_x$-Pt/OMC electrocatalysts were systematically controlled. The three samples with different amounts of $SbO_x$ were named $SbO_x$-Pt/OMC-n (n = 1, 2, and 3) to effectively differentiate each electrocatalyst by the amount of $SbO_x$. The higher value of n indicates a higher amount $SbO_x$. The incorporation of amorphous antimony oxide ($SbO_x$) on Pt/OMC was also performed *via* a wet impregnation method. For synthesis of $SbO_x$-Pt/OMC-1, $SbO_x$-Pt/OMC-2, and $SbO_x$-Pt/OMC-3, 0.10, 0.17, and 0.23 g of antimony chloride was used, respectively. The prepared antimony chloride was dissolved in 1.5 mL of anhydrous acetone. This antimony precursor solution was dropped onto as-prepared 0.5 g of Pt/OMC electrocatalyst and impregnated by grinding in a mortar. The subsequent series of synthetic processes (*i.e.,* drying and heat-treatment) were the same as in Pt/OMC.

## 2.4. Material characterization

To characterize the crystal structure of each electrocatalyst, X-ray diffraction (XRD, Rigaku D/Max 2200 V) analysis was used. Nitrogen physisorption-desorption analysis (Micromeritics ASAP 2420) was also performed at 77 K to investigate the porous architectures of the as-prepared electrocatalysts. To characterize the valence state of the electrocatalysts, X-ray photoelectron spectroscopy (XPS, Thermo Fisher Scientific K-Alpha+ XPS) was carried out. The deconvolution of XPS was performed by using peak fitting program based on the spin-orbit splitting theory. The overall binding energy of XPS spectra were corrected with reference to C 1s spectra (284.8 eV). The detailed electronic structures of each electrocatalyst were studied by X-ray absorption spectroscopy (XAS) analysis using a 7D X-ray absorption fine structure

(XAFS) beamline at the Pohang Accelerator Laboratory (PAL, Republic of Korea). Scanning electron microscopy (SEM, Tescan Mira3 LMU, transmission electron microscopy (TEM, Themo Fisher Scientific Talos F200S) and spherical aberration-corrected TEM (Cs-TEM, FEI Titan cubed G2 60–300) were used to investigate the particle morphology of the electrocatalysts. The elemental mappings were performed by energy dispersive X-ray spectrometer (EDS) attached to the TEM equipment. The metal content of the electrocatalysts was analyzed by thermogravimetric analysis (TGA, TA instruments SDT Q600) and inductively coupled plasma mass spectrometer (ICP-MS, PerkinElmer NexION1000).

## 2.5. Electrochemical measurements

A glassy carbon electrode (GCE, 5 mm diameter) was used as a working electrode to characterize the kinetic properties of each electrocatalyst. It is because that glassy carbon is favorable for the formation of flat and thin electrocatalyst layer, so other side factors which can disturb exact interpretation of the kinetic properties of electrocatalysts can be controlled. The GCE was polished with an aqueous diamond/ alumina suspension on a polishing cloth before the electrochemical test. Electrocatalyst ink was prepared by following steps: 8 mg of electrocatalyst (Pt/C, Pt/OMC, and $SbO_x$-Pt/OMC electrocatalysts) was mixed with 400 μL of DI-water and 40 μL of Nafion® solution. After homogeneously mixing, 1.6 mL of IPA was added to the electrocatalyst ink and sonicated for 3 h to accomplish the perfect dispersion of electrocatalysts. Then, 10 μL of electrocatalyst ink was dropped on the GCE, and dried for 30 min. The total amount of electrocatalyst on the GCE was controlled to 0.04 mg (*i.e.,* areal loading amount of 0.1998 mg cm$^{-2}$). A cyclic voltammetry (CV) test was performed in three electrode half-cell reactors using a potentiostat (ZIVE MP1, WonATech). Pt wire and Ag/AgCl (1.0 M KCl) were used as counter and reference electrodes, respectively. $H_{upd}$ measurements were used to investigate the electrochemical surface area (ECSA) of the Pt. To measure the ECSA of the electrocatalysts, 0.5 M of $H_2SO_4$ solution was used as an electrolyte. Before measuring the ECSA, Ar gas was purged for 30 min. During the measurement of the ECSA, Ar gas was continuously purged. All CV data for the ECSA was collected in the potential range of 0.05–1.25 V (*vs.* RHE) with a scan rate of 50 mV s$^{-1}$. The ECSA was calculated by the following equation:[31].

$$ECSA \quad \left( m^2 \quad g_{Pt}^{-1} \right) = \frac{Q_H}{q \times [Pt]}$$

where $Q_H$ is the charge for hydrogen desorption, q is the monolayer hydrogen desorption charge (210 μC cm$^{-2}$) [32,33], and [Pt] is the total amount of platinum loaded on the electrode. The ECSA was also estimated by CO stripping voltammetry. Before measuring the ECSA, Ar gas was purged for 30 min. During the measurement of the ECSA, Ar gas was continuously purged and CV data was collected in the potential range of 0.05–1.25 V (*vs.* RHE) with a scan rate of 50 mV s$^{-1}$. After stopping the purging of Ar gas, CO gas was purged for 20 min at the constant potential of 0.1 V (*vs.* RHE). After stopping the purging of CO gas, Ar gas was purged again for 1 h at the same potential. CV data was collected in the potential range of 0.05–1.25 V (*vs.* RHE) with a scan rate of 50 mV s$^{-1}$ by purging the Ar gas continuously. To evaluate electrocatalytic activity of electrocatalysts by CV analysis, 2.0 M glycerol in a 0.5 M $H_2SO_4$ solution was used as electrolyte. Before the CV analysis, Ar gas was purged for 30 min to completely remove the dissolved $O_2$ gas. For the calibration of the reference electrode, the Pt rotating disk electrode (RDE, 5 mm diameter) and Pt wire were used as working and counter electrodes, respectively, in a hydrogen-saturated 0.5 M $H_2SO_4$ electrolyte. The calibration resulted in a shift of − 0.253 V (*vs.* RHE) for 0.5 M $H_2SO_4$ electrolyte. All potential values were calibrated to the reversible hydrogen electrode (RHE) using $E$ (RHE) $= E_{Ag/AgCl}$ + 0.253 V. During the CV analysis, Ar gas was continuously purged. The CV test was performed in the potential range of 0.05–1.25 V (*vs.* RHE) at

a scan rate of 50 mV s$^{-1}$. To perform an accelerated durability test (ADT), CV analysis was performed for 1000 cycles in the potential range of 0.05–1.25 V (*vs.* RHE) at a scan rate of 50 mV s$^{-1}$.

### 2.6. EGOR and product analysis

EGOR was performed through a chronoamperometry (CA) test at 0.920 V (*vs.* RHE) by using a three-electrode half-cell reactor and potentiostat. Pt wire and Ag/AgCl (1.0 M KCl) were used as counter and reference electrodes, respectively. Electrocatalyst coated Ti paper (Bekaert) was used as a working electrode for the characterization of EGOR products. It is because that the use of Ti paper as porous transport layer is favorable to increase both areal loading amount of electrocatalysts and contact area of electrocatalysts with electrolyte, resulting in reliable production of EGOR products. Electrocatalysts were mixed with DI-water and Nafion® solution by vortexing. Then, IPA was added to the as-prepared electrocatalyst solution and sonicated for 3 h. After the sonication, the electrocatalyst solution was coated on the Ti paper electrode with a geometric area of 2 cm$^2$ and an electrocatalyst loading amount of 2.5 mg cm$^{-2}$ *via* a spray coating method. The electrocatalyst coated Ti paper was dried in an oven at 110 ℃ overnight. The 0.1 M glycerol in a 0.5 M H$_2$SO$_4$ solution was used as the electrolyte and the 7 mL of electrolyte was stirred at 300 rpm and maintained at 60 ℃ during the EGOR. Before the CA test, the electrolyte was purged with Ar gas for 30 min to completely remove the O$_2$ gas dissolved in electrolyte. High performance liquid chromatography (HPLC, YL9100, YL Instruments) analysis was performed to characterize the products which were produced from the EGOR process. A refractive index detector (RI-201 H, Shodex) and a UV-Vis Detector (210 nm, UV/Vis, YL9120, YL Instruments) were used. A Hi-Plex H column (Agilent Technologies) and a column oven (At-4500, Futecs) were used with 0.005 M H$_2$SO$_4$ solution as an eluent at 50 ℃ with a flow rate of 0.3 mL min$^{-1}$. Then 10 μL of reacted mixture was filtered by a 0.2 μm filter and injected by an auto sampler. The amount of reacted glycerol and product yields were quantified by an external calibration method. The glycerol conversion ($X_{Gly}$) and product selectivity ($S_P$) were calculated by following equation:

$$X_{Gly}(\%) = \frac{n_{Gly,in} - n_{Gly,out}}{n_{Gly,in}} \times 100$$

$$S_P(\%) = \frac{n_{P,out}}{n_{Gly,in} - n_{Gly,out}} \times 100$$

To characterize the long-term stability of electrocatalysts, EGOR was performed by CA techniques for 120 h under the same cell operating conditions with aforementioned CA test. We changed electrolyte to new one and analysed EGOR products by HPLC every 24 h.

### 2.7. DFT calculations

All the first-principles of density functional theory (DFT) calculations were performed with the Vienna *ab-initio* simulation package (VASP) [34]. Spin-polarized DFT and the generalized gradient approximation [35] with the Perdew–Burke–Ernzerhof (PBE) exchange-correlation functionals were employed. The projector-augmented wave (PAW) method [36] was used to describe electron core pseudo-potentials. A kinetic energy cutoff of 500 eV and $3 \times 3 \times 1$ $k$ point was used in all the structural minimization. The convergences of energy and force were set as $10^{-5}$ eV and 0.02 eV Å$^{-1}$, respectively. A vacuum region of 15 Å was set to avoid artificial interactions between the periodically repeated unit cells. The charge density differences were evaluated using the formula $\Delta\rho = \rho_{slab+ads} - \rho_{slab} - \rho_{ads}$, where $\rho_{slab}$, $\rho_{ads}$, and $\rho_{slab+ads}$ are the electron densities of the Pt (or SbO$_x$-Pt) slab, the adsorbate, and the adsorption state structure, respectively. We employed a three-layered $5 \times 5$ supercell to simulate the Pt electrocatalyst, incorporating a total of 75 Pt atoms. The bottom layer was kept fixed to accurately represent the bulk

region. To model Sb$_2$O$_3$ clusters on the Pt surface, we utilized a structure consisting of four Sb atoms and six oxygen atoms. In order to account for solvation effects and the formation of glycerol-water adducts through the dissociation of water molecules, we considered the presence of one water molecule surrounding glycerol.

## 3. Results and discussion

### 3.1. Design of an OMC-supported SbO$_x$-Pt electrocatalyst

Recently, it has been revealed that the overall electrochemistry of EGOR is highly dependent on the physical and chemical properties of carbon support materials [21]. In particular, the porous architecture of a carbon support has been considered as an important factor in determining the electrocatalytic activity and selectivity of the electrocatalyst in EGOR. Here, OMC with well-developed cylindrical mesopores was used as a support material to design a highly efficient electrocatalyst. The cylindrical mesopores, which have low tortuosity and large pore size ($> 2$ nm), are favorable for the facile mass transfer of active species, which is usually limited in activated carbon with tortuous small micropores ($< 2$ nm) (Fig. S3). Further, the high surface area of OMC allows the electrocatalysts to be uniformly dispersed on the surface of the support materials, which inhibits the aggregation of electrocatalysts, and accelerates the electrocatalysis. For this, we used the EISA method [37] to synthesize an OMCS composite, and OMC was prepared by etching the silica of the OMCS (see experimental). N$_2$ adsorption-desorption analysis was performed to investigate the porous structures of the OMCS and OMC (Fig. 2a and b). The isotherm linear plots of OMCS and OMC are type-IV with distinguished capillary condensation phenomena at the P/P$_o$ of ~0.6, indicating the well-developed mesopores (Fig. 2a). The OMC has a high Brunauer-Emmett-Teller (BET) surface area of 1268 m$^2$ g$^{-1}$, whereas BET specific surface area of OMCS is 370 m$^2$ g$^{-1}$. The removal of silica during the etching process leads to the small amount of the formation of 3–4 nm sized mesopores in OMC, which increases the specific surface area. The Barrett-Joyner-Halenda (BJH) pore size distribution of OMC and OMCS was dominantly centered at 6 nm, indicating that F127 derived mesopore of 6 nm was well-maintained even after etching process (Fig. 2b). The TEM image of OMC also shows the ordered mesoporous architecture with a 6 nm size, which is consistent with N$_2$ physisorption analysis results (Fig. 2c). We believe that as-prepared OMC with high surface area and well-developed mesopores is suitable as a support material for EGOR electrocatalysts. Meanwhile, a SbO$_x$ incorporated Pt nanoparticle electrocatalyst was introduced into the OMC support material (SbO$_x$-Pt/OMC) to design promising electrocatalysts for EGOR. The amount of SbO$_x$ was systematically controlled to correlate the effect of SbO$_x$ incorporation on the Pt surface and EGOR performance. Each SbO$_x$-Pt/OMC electrocatalyst with different amounts of SbO$_x$ is named SbO$_x$-Pt/OMC-n (n = 1, 2, and 3). A higher value of n indicates a higher amount of SbO$_x$. For example, ICP-MS analysis results showed that the Sb contents in SbO$_x$-Pt/OMC-1, SbO$_x$-Pt/OMC-2, and SbO$_x$-Pt/OMC-3 were 10.9, 15.0, and 16.4 wt%, respectively (Table S1). The composite of OMC and the Pt nanoparticle electrocatalyst without any incorporation of SbO$_x$ (Pt/OMC) and Pt/C were used as a control group. For fair comparison, the weight ratio of Pt to the carbon support was fixed at 2:8 in all the electrocatalysts (Fig. S4). The ICP-MS analysis results revealed that the Pt content of Pt/C and Pt/OMC were approximately 20 wt%, whereas the contents of Pt decreased as the amount of SbO$_x$ increased in the SbO$_x$-Pt/OMC electrocatalysts (Table S1). The TGA results also well-matched with those of ICP-MS, showing that ~20 wt% of the total weight remained in Pt/C and Pt/OMC after the carbon support was removed (Fig. S5 and Table S2). In the SbO$_x$-Pt/OMC electrocatalysts, more of the total weight remained as the amount of SbO$_x$ increased.

To characterize the morphological features of Pt/C, Pt/OMC, and SbO$_x$-Pt/OMC electrocatalysts, TEM, high angle annular dark field-
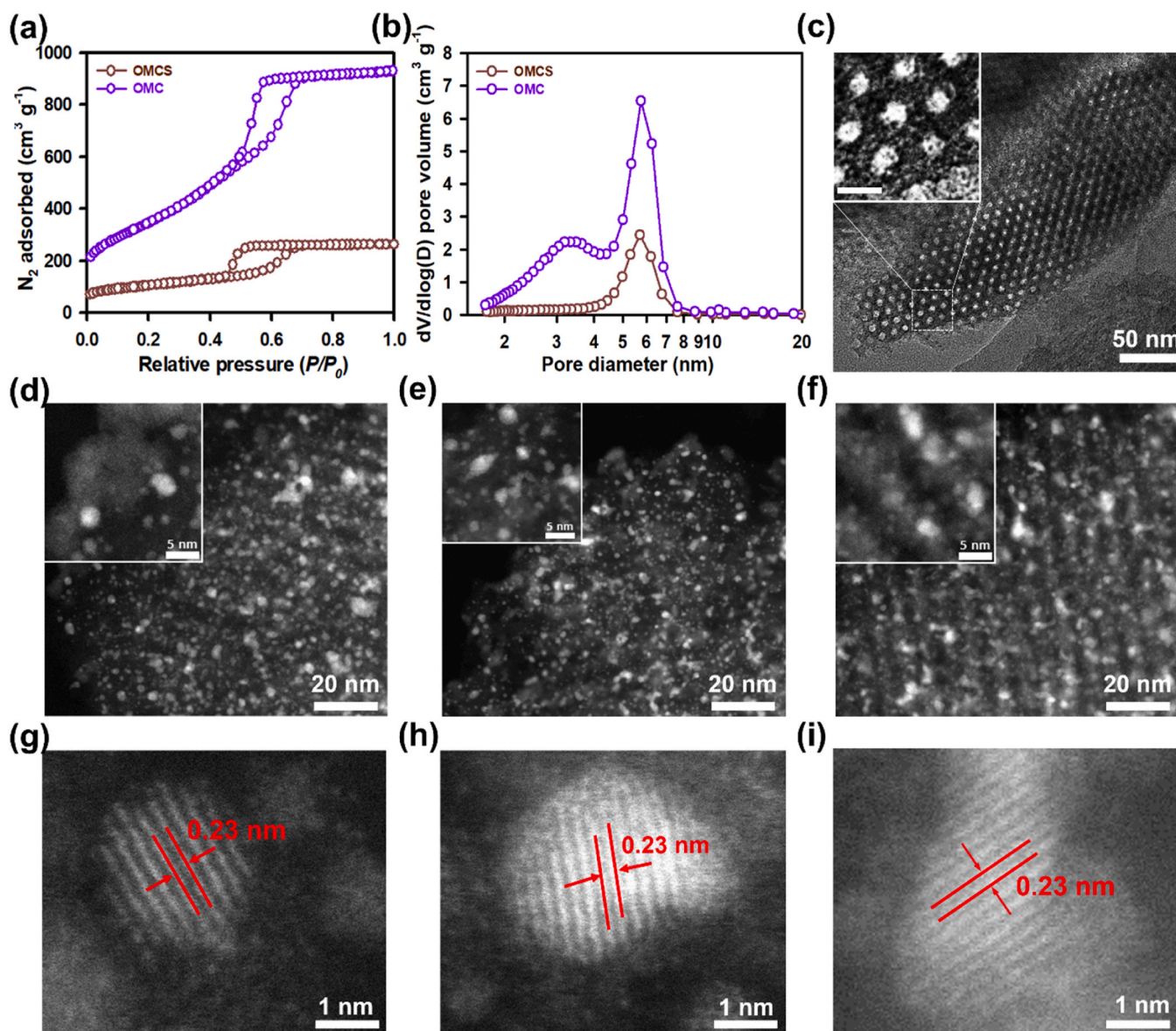
**Fig. 2.** (a) The isotherm linear plots and (b) pore size distribution plots of OMCS and OMC. (c) TEM image of the OMC support (Scale bar of inset image: 10 nm). HAADF-STEM images of (d) $SbO_x$-Pt/OMC-1, (e) $SbO_x$-Pt/OMC-2, and (f) $SbO_x$-Pt/OMC-3. High-resolution STEM images of (g) $SbO_x$-Pt/OMC-1, (h) $SbO_x$-Pt/OMC-2, and (i) $SbO_x$-Pt/OMC-3.

scanning TEM (HAADF-STEM), and EDS analyses were performed. The TEM images of Pt/C and Pt/OMC showed that Pt nanoparticles are homogeneously dispersed on the carbon support (Fig. S6). The Pt particle size distribution of Pt/C and Pt/OMC were centered at ~2.4 and ~1.8 nm, respectively (Fig. S7). In the case of $SbO_x$-Pt/OMC, electrocatalyst nanoparticles were still well-dispersed on the OMC support even after the $SbO_x$ incorporation process (Fig. 2d-f). The Pt particle size distribution of $SbO_x$-Pt/OMC-1, $SbO_x$-Pt/OMC-2, and $SbO_x$-Pt/OMC-3 were 1.9, 1.8, and 2.0 nm, respectively (Fig. S8). The high-resolution STEM images of $SbO_x$-Pt/OMC revealed nanoparticles with a lattice fringe of 0.23 nm which corresponded to the (111) plane of Pt (Fig. 2g-i). On the other hand, other lattice fringes that matched the crystalline structures of $SbO_x$ were not observed in any of the $SbO_x$-Pt/OMC electrocatalysts, which suggested the possibility that the $SbO_x$ deposited on the surface of the Pt nanoparticles was amorphous. HAADF-STEM images with EDS mapping of Pt and Sb indicated that Pt nanoparticles were uniformly dispersed on the surface of the OMC support and $SbO_x$ particles were well-incorporated into the surfaces of the Pt nanoparticles (Fig. 3a-c). XRD analysis was used to further investigate the crystalline

structure of the electrocatalysts. Three crystalline peaks at 39°, 46°, and 67°, which respectively corresponded to the (111), (200), and (220) planes of face-centered cubic (fcc) structured Pt [38,39], are observed in the XRD patterns of Pt/C (Fig. S9) and Pt/OMC (Fig. 3b). The XRD patterns of $SbO_x$-Pt/OMC electrocatalysts had the broad crystalline peaks of Pt, indicating a crystallinity decrease in the Pt nanoparticles by incorporation of $SbO_x$ on the Pt surface, which is attributed to the strong interaction between $SbO_x$ and Pt particles [40]. More importantly, XRD patterns of $SbO_x$-Pt/OMC exhibited only Pt crystalline peaks without any other crystalline peaks corresponding to $SbO_x$, which was consistent with the electron microscopy analysis result.

The chemical states of $SbO_x$-Pt/OMC electrocatalysts were investigated using XPS analysis. XPS survey plots of Pt/C and Pt/OMC showed Pt 4f peaks at ~72.0 eV, C 1s peaks at ~285.0 eV, and O 1s peaks at ~532.0 eV (Fig. 3c). In the case of three $SbO_x$-Pt/OMC electrocatalysts, Sb 3d peaks in the binding energy range of 530.0–540.0 eV were observed in addition to Pt 4f, C 1s, and O 1s peaks. In particular, the Sb 3d spectra of $SbO_x$-Pt/OMC had the characteristic peaks of $Sb^{3+}$ (i.e., $Sb^{3+}$ $3d_{3/2}$ and $Sb^{3+}$ $3d_{5/2}$) and $Sb^0$ (i.e., $Sb^0$ $3d_{3/2}$ and $Sb^0$ $3d_{5/2}$)
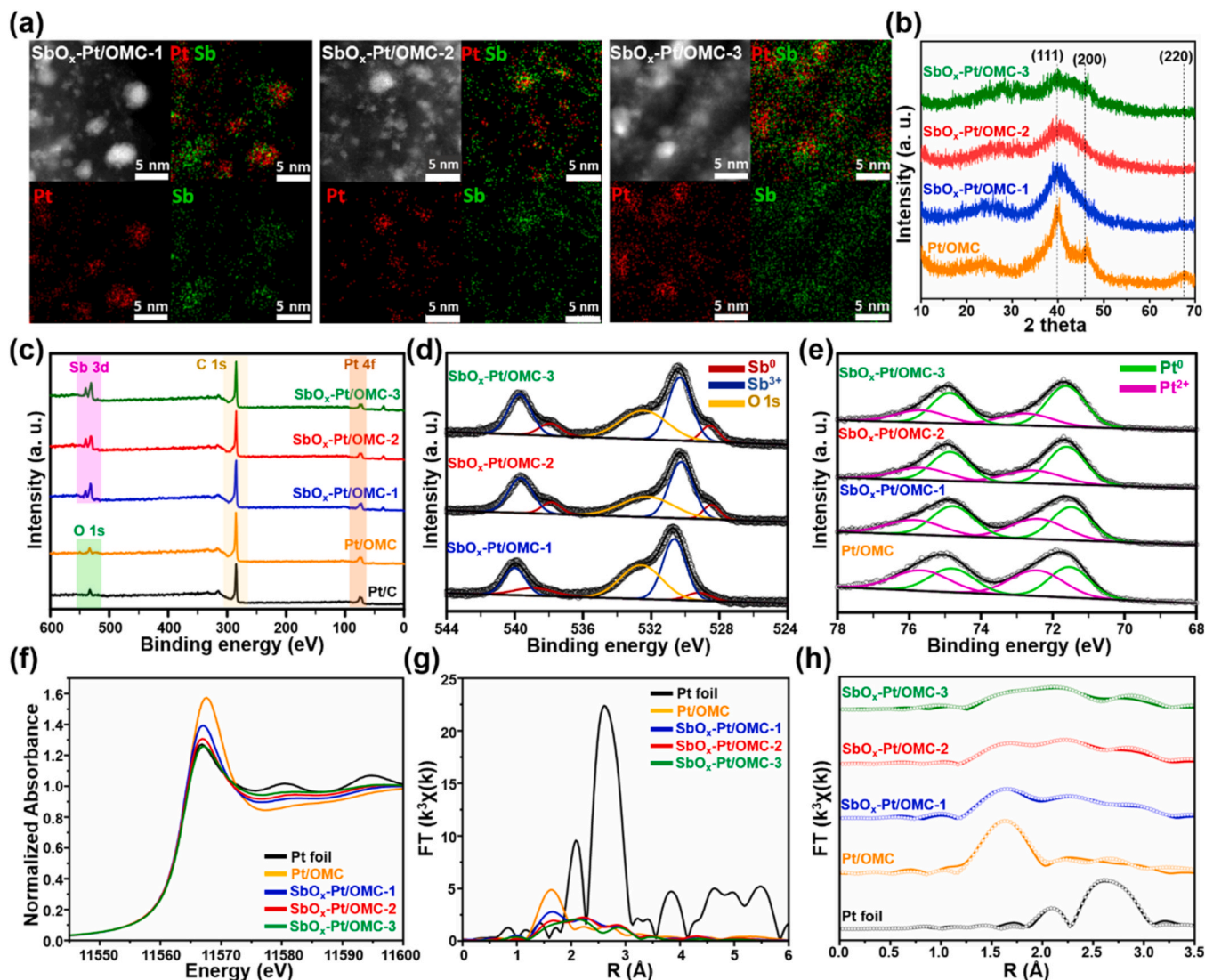
**Fig. 3.** (a) HAADF-STEM and EDS mapping images of $SbO_x$-Pt/OMC electrocatalysts. (b) XRD patterns of Pt/OMC and $SbO_x$-Pt/OMC electrocatalysts. (c) XPS survey spectra of Pt/C, Pt/OMC, and $SbO_x$-Pt/OMC electrocatalysts. (d) Sb 3d XPS spectra of $SbO_x$-Pt/OMC electrocatalysts. (e) Pt 4f XPS spectra of Pt/OMC and $SbO_x$-Pt/OMC electrocatalysts. (f) XANES spectra, (g) $k^3$-weighted FT-EXAFS spectra, and (h) fitted FT-EXAFS curves of Pt foil, Pt/OMC, and $SbO_x$-Pt/OMC electrocatalysts at the Pt $L_3$ edge.

(Fig. 3d and Table S3) [41,42]. The Sb 3d spectra of $SbO_x$-Pt/OMC clearly suggested that $Sb^{3+}$ was a dominant oxidation state of $SbO_x$ in $SbO_x$-Pt/OMC. For instance, the calculated areas under the curve (AUC) ratio of $Sb^{3+}$ were 65.80%, 79.12%, and 76.53% in $SbO_x$-Pt/OMC-1, $SbO_x$-Pt/OMC-2, and $SbO_x$-Pt/OMC-3 (Table S3). It indicated that the $SbO_x$ nanoparticles in $SbO_x$-Pt/OMC were most likely composed of amorphous $Sb_2O_3$ [43,44]. On the other hand, the Pt 4f spectra of Pt/C, Pt/OMC, and $SbO_x$-Pt/OMC exhibited the characteristic peaks of $Pt^{2+}$ (i. e., $Pt^{2+}$ $4f_{7/2}$ and $Pt^{2+}$ $4f_{5/2}$) and $Pt^0$ (i.e., $Pt^0$ $4f_{7/2}$ and $Pt^0$ $4f_{5/2}$) (Fig. 3e and S10). It is noteworthy that the AUC ratio of $Pt^0$ increased as the amount of $SbO_x$ increased in $SbO_x$-Pt/OMC (e.g., $SbO_x$-Pt/OMC-3 had the highest AUC of $Pt^0$: 71.55%) (Table S3). The relatively low valence state of Pt in the $SbO_x$-Pt/OMC electrocatalyst was due to the strong interaction between Pt and $SbO_x$ nanoparticles with electron transfer from $SbO_x$ to Pt [17,45,46]. The local atomic structures and electronic states of the $SbO_x$-Pt/OMC electrocatalysts were thoroughly characterized by XAS analysis. In X-ray absorption near edge structure (XANES) spectra, Pt/OMC had a higher white line intensity compared to Pt foil, indicating more vacancies in the valence orbital, in other words, a more oxidized electronic structure in Pt/OMC than in Pt foil (Fig. 3f). The white line intensity decreased as the amount of $SbO_x$ increased, and

$SbO_x$-Pt/OMC-3 exhibited a white line intensity similar to Pt foil. Therefore, the electron transfer from $SbO_x$ to Pt could be further supported by XANES analysis. In the extended X-ray absorption fine structure (EXAFS) spectra, the formation of a Pt-Sb bond in the $SbO_x$-Pt/OMC electrocatalysts was confirmed by a new peak that appeared at 2.3 Å, which validated the well-incorporated $SbO_x$ particles on the Pt surfaces (Fig. 3g). Furthermore, the peak intensity of the Pt-O bond at 1.6 Å, which was due to the bonding with surface adsorbed oxygen ligands, decreased as the amount of $SbO_x$ increased. A decreased coordination number of the Pt-O bond was observed in the fitting result of the EXAFS spectra (Fig. 3h and Table S4). Comprehensively, series of material characterizations including EXAFS results manifest that amorphous $SbO_x$ was well loaded on the surface of Pt nanoparticle in $SbO_x$-Pt/OMC electrocatalyst.

Meanwhile, the BET surface areas of the Pt/OMC and Pt/C electrocatalysts were 860 and 176 $m^2$ $g^{-1}$, respectively (Fig. S11a and Table S5). After the incorporation of $SbO_x$ nanoparticles, the specific surface area of electrocatalysts gradually decreased. $SbO_x$-Pt/OMC-1, $SbO_x$-Pt/OMC-2, and $SbO_x$-Pt/OMC-3 exhibited specific surface areas of 718, 713, and 691 $m^2$ $g^{-1}$, respectively (Table S5). The decrease of specific surface in $SbO_x$-Pt/OMC electrocatalysts is attributed to the

partial cover of Pt surface by amorphous SbO$_x$ particles. Despite the lower surface area of SbO$_x$-Pt/OMC than Pt/OMC, pore size distributions of Pt/OMC and SbO$_x$-Pt/OMC were identically centered at 6 nm (Fig. S11b), implying that porous structures of the OMC support were well maintained even after deposition of amorphous SbO$_x$ in the Pt nanoparticle surface.

### 3.2. Study on electrocatalytic activity and stability of electrocatalysts

The electrocatalytic activity and stability of as-prepared electrocatalysts were evaluated using a series of electrochemical tests. First, the ECSA was estimated using CV analysis at a scan rate of 50 mV s$^{-1}$ in a 0.5 M H$_2$SO$_4$ electrolyte without glycerol (Fig. 4a). Based on the desorption of underpotentially deposited hydrogen (H$_{upd}$), the ECSA of the Pt/C and Pt/OMC electrocatalysts were 69 and 60 m$^2$ g$_{Pt}^{-1}$, respectively (Table S6). On the other hand, SbO$_x$-Pt/OMC electrocatalysts had lower ECSA than those of Pt/C and Pt/OMC. The ECSA of SbO$_x$-Pt/OMC-1, SbO$_x$-Pt/OMC-2, and SbO$_x$-Pt/OMC-3 were 49, 42, and 39 m$^2$ g$_{Pt}^{-1}$, respectively. Further, ECSA was also estimated by CO stripping voltammetry (Fig. S12 and Table S6). The overall value and tendency of ECSA were almost similar with those of ECSA collected from H$_{upd}$

desorption; the Pt/C showed the highest ECSA (77 m$^2$ g$_{Pt}^{-1}$), whereas SbO$_x$-Pt/OMC-3 showed the lowest ECSA (49 m$^2$ g$_{Pt}^{-1}$). The decrease of ECSA in SbO$_x$-Pt/OMC was because the surface of the Pt nanoparticles was partially covered by amorphous SbO$_x$ particles. As a result, SbO$_x$-Pt/OMC-3 with the highest amount of SbO$_x$ showed the lowest ECSA. The electrocatalytic activity was further evaluated by CV analyses at a scan rate of 50 mV s$^{-1}$ using 2.0 M glycerol in a 0.5 M H$_2$SO$_4$ solution as an electrolyte, and specific activity (*i.e.,* maximum current density per ECSA) and mass activity (*i.e.,* maximum current density per Pt mass) were established from a geometric current density plot (Fig. S13) to accurately investigate the electrocatalytic activity of SbO$_x$-Pt/OMC electrocatalysts (Fig. 4b and c). First, the specific activity of Pt/OMC (0.3410 mA cm$_{ECSA}^{-2}$) was slightly higher than that of Pt/C (0.2809 mA cm$_{ECSA}^{-2}$), suggesting that OMC could be a favorable support material for EGOR (Fig. 4b and Table S6). Most importantly, all the SbO$_x$-Pt/OMC electrocatalysts demonstrated significantly higher specific activity than Pt/OMC, suggesting that amorphous SbO$_x$ on a Pt surface could affect the reaction by directly interacting with the reaction intermediates and/or by inducing the electronic effect of surface Pt. In particular, SbO$_x$-Pt/OMC-3 exhibited the highest specific activity (0.6754 mA cm$_{ECSA}^{-2}$, ~1.5 and ~1.1 times higher than those of SbO$_x$-Pt/
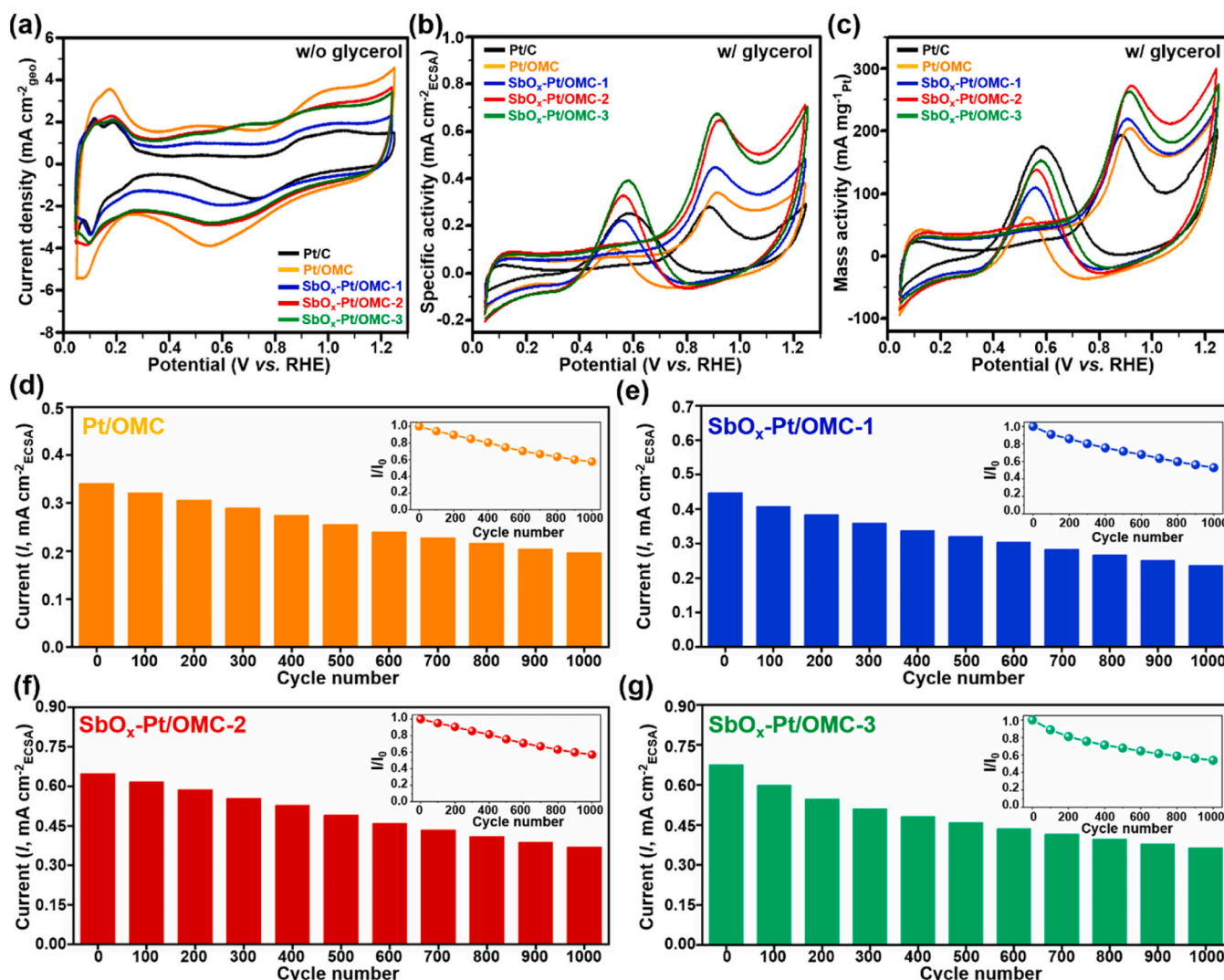


**Fig. 4.** (a-c) CV curves of each electrocatalyst at a scan rate of 50 mV s$^{-1}$. (a) Geometric current density. For estimating ECSA by this CV analysis, 0.5 M H$_2$SO$_4$ electrolyte without glycerol was used. (b) Specific activity, and (c) mass activity of Pt/C, Pt/OMC, and SbO$_x$-Pt/OMC electrocatalysts. For estimating electrocatalytic activity by these CV analyses, 2.0 M glycerol in 0.5 M H$_2$SO$_4$ electrolyte was used. The specific activity of (d) Pt/OMC, (e) SbO$_x$-Pt/OMC-1, (f) SbO$_x$-Pt/OMC-2, and (g) SbO$_x$-Pt/OMC-3 electrocatalysts with different numbers of cycles. The inset figures provided in (d-g) indicate the $I/I_0$ values of each electrocatalyst with different numbers of cycles.

OMC-1 and SbO$_x$-Pt/OMC-2, respectively) among the SbO$_x$-Pt/OMC electrocatalysts. In the case of mass activity, the SbO$_x$-Pt/OMC electrocatalysts exhibited higher value than Pt/OMC and Pt/C (Fig. 4c and Table S6). The SbO$_x$-Pt/OMC-2 exhibited higher mass activity (272.3 mA mg$_{Pt}^{-1}$) than SbO$_x$-Pt/OMC-1 (219.4 mA mg$_{Pt}^{-1}$) and SbO$_x$-Pt/OMC-3 (263.4 mA mg$_{Pt}^{-1}$). Consequently, the amount of amorphous SbO$_x$ on the Pt surface had a linear and volcano relationship with the specific activity and mass activity of Pt, respectively (Fig. S14). Therefore, careful control of the deposition amount of SbO$_x$ particle to moderate level on a Pt surface is necessary for optimizing the electrocatalytic activity of the EGOR process.

In addition to electrocatalytic activity, we also studied the stability of each electrocatalyst by an ADT of CV cycling at a scan rate of 50 mV s$^{-1}$ for 1000 cycles. First, an *ex-situ* TEM image of Pt/C after an ADT showed severe aggregation of Pt nanoparticles (Fig. S15). On the other hand, *ex-situ* TEM images of Pt/OMC and SbO$_x$-Pt/OMC electrocatalysts with OMC support materials revealed that Pt nanoparticles were still well-dispersed on the carbon surface without severe aggregation even after an ADT (Fig. S16). Further, the *ex-situ* XRD pattern of Pt/C after the ADT revealed a different sharpness of the crystalline Pt peaks compared with that of before the ADT (Fig. S17). After the ADT, the sharpness of the Pt crystalline (200) plane peak at ~46° increased significantly in Pt/C

owing to an increase of the Pt crystallite size with severe particle aggregation. In the case of Pt/OMC and SbO$_x$-Pt/OMC electrocatalysts, Pt crystalline (200) plane peaks after the ADT showed a relatively similar sharpness as those of before the ADT, implying that an OMC support is favorable for inhibiting the aggregation of electrocatalyst particles during the EGOR process. To quantitatively characterize the electrocatalyst stability, the current ratio of the measured value after cycling ($I$) and the measured value at the 1st cycle ($I_0$) was estimated from the CV analyses at different cycles. In the case of Pt/C, the $I/I_0$ ratio sharply decreased as the cycle progressed and consequently reached 0.43 after 1000 cycles (Fig. S18). The Pt/OMC exhibited more stable retention of the $I/I_0$ ratio than Pt/C (Fig. 4d and Table S7). The $I/I_0$ ratio of Pt/OMC was 0.58 even after 1000 cycles, suggesting that an OMC support has the potential to enhance the stability of electrocatalysts. In the case of SbO$_x$-Pt/OMC electrocatalysts, the $I/I_0$ values of the SbO$_x$-Pt/OMC electrocatalyts were similar to that of Pt/OMC and significantly higher than that of Pt/C (Fig. 4e-g). It implies that porous structure of support carbon materials is one of the most critical factors to determine the stability of electrocatalysts during EGOR.
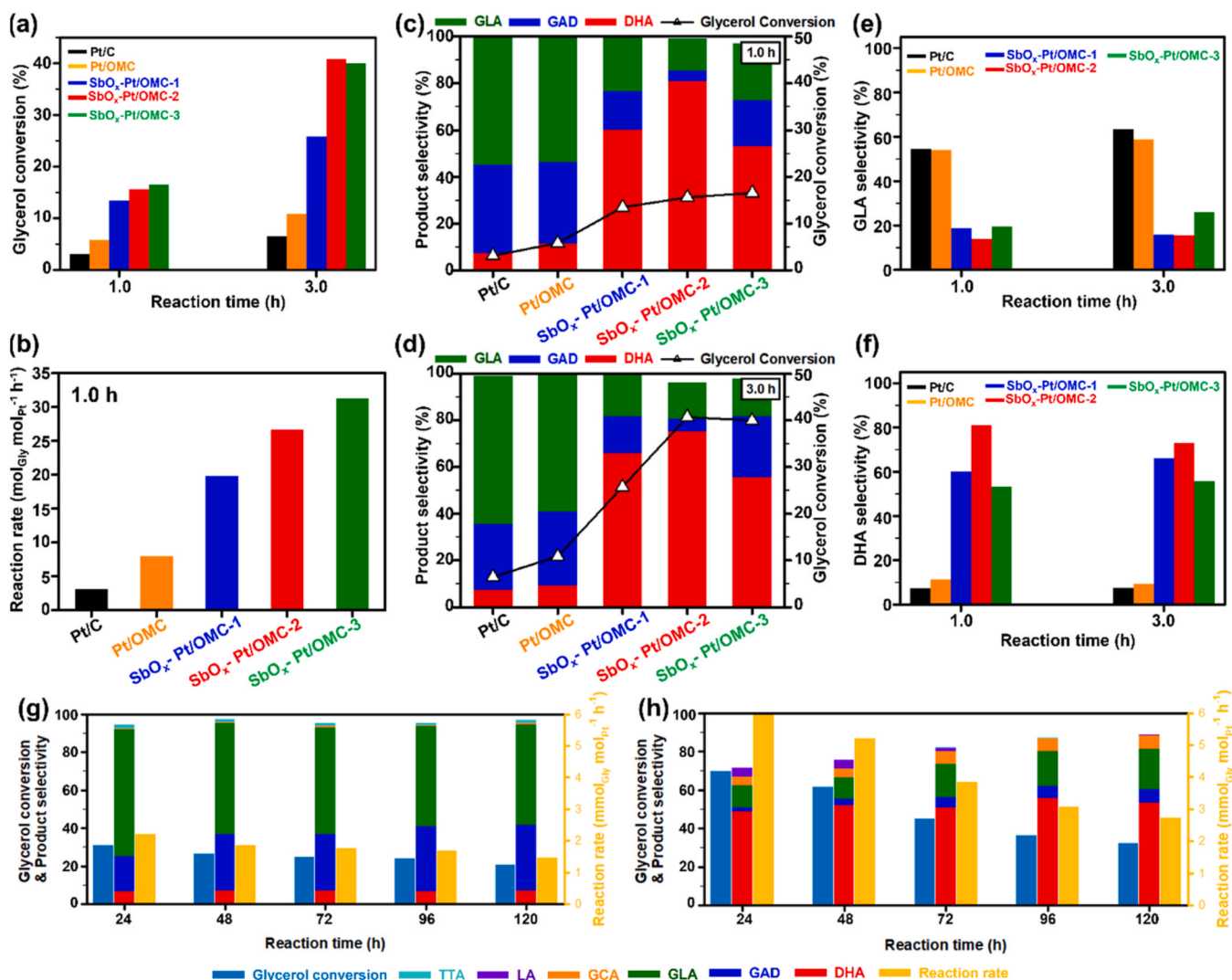


**Fig. 5.** (a) Glycerol conversion of Pt/C, Pt/OMC, and SbO$_x$-Pt/OMC electrocatalysts at different reaction times of 1 and 3 h. (b) Reaction rate of Pt/C, Pt/OMC, and SbO$_x$-Pt/OMC electrocatalysts at a reaction time of 1 h. The product selectivity and overall glycerol conversion of Pt/C, Pt/OMC, and SbO$_x$-Pt/OMC electrocatalysts at a reaction time of (c) 1 and (d) 3 h. (e) GLA selectivity and (f) DHA selectivity of Pt/C, Pt/OMC, and SbO$_x$-Pt/OMC electrocatalysts at different reaction times of 1 and 3 h. The long-term CA test results for (g) Pt/C and (h) SbO$_x$-Pt/OMC-2.

## 3.3. Study on product and selectivity of electrocatalysts

To characterize the products and selectivity of each electrocatalyst for the EGOR process, a CA test at 0.920 V (*vs.* RHE) followed by a HPLC analysis was performed using electrocatalyst coated Ti paper as a working electrode (Fig. S19). After 1 and 3 h, glycerol conversion of Pt/OMC (*i.e.,* 5.8% and 10.9% at 1 and 3 h, respectively) was higher than that of Pt/C (*i.e.,* 3.1% and 6.5% at 1 and 3 h, respectively) which was similar to the CV results (Fig. 5a and Table S8). Meanwhile, $SbO_x$-Pt/OMC electrocatalysts showed much higher conversion of glycerol than Pt/OMC after 1 and 3 h. For example, glycerol conversion of $SbO_x$-Pt/OMC-1, $SbO_x$-Pt/OMC-2, and $SbO_x$-Pt/OMC-3 after 1 h were 13.5%, 15.6%, and 16.5%, respectively, which were much higher than that of Pt/OMC (5.8%). After 3 h, $SbO_x$-Pt/OMC-1, $SbO_x$-Pt/OMC-2, and $SbO_x$-Pt/OMC-3 exhibited a glycerol conversion of 25.8 (2.4 times higher than Pt/OMC), 40.8 (3.7 times higher than Pt/OMC), and 40.0% (3.6 times higher than Pt/OMC), respectively. Beyond high glycerol conversion, $SbO_x$-Pt/OMC electrocatalysts also exhibited an improved reaction rate per Pt mole of the EGOR process for 1 and 3 h (Fig. 5b and S20). After 1 h, $SbO_x$-Pt/OMC-1 (19.80 $mol_{Gly}$ $mol_{Pt}^{-1}$ $h^{-1}$), $SbO_x$-Pt/OMC-2 (26.70 $mol_{Gly}$ $mol_{Pt}^{-1}$ $h^{-1}$), and $SbO_x$-Pt/OMC-3 (31.27 $mol_{Gly}$ $mol_{Pt}^{-1}$ $h^{-1}$) experienced much higher reaction rates than those of Pt/C (3.12 $mol_{Gly}$ $mol_{Pt}^{-1}$ $h^{-1}$) and Pt/OMC (7.94 $mol_{Gly}$ $mol_{Pt}^{-1}$ $h^{-1}$) (Fig. 5b). After 3 h, the reaction rates of $SbO_x$-Pt/OMC-1, $SbO_x$-Pt/OMC-2, and $SbO_x$-Pt/OMC-3 were still 12.47, 23.54, and 24.89 $mol_{Gly}$ $mol_{Pt}^{-1}$ $h^{-1}$, respectively, whereas those of Pt/C and Pt/OMC were 4.33 and 5.01 $mol_{Gly}$ $mol_{Pt}^{-1}$ $h^{-1}$, respectively (Fig. S20). This result confirmed that the synergistic effect of using an OMC support and the incorporation of amorphous $SbO_x$ on a Pt surface can increase the glycerol conversion during the EGOR process (Fig. S21).

In the case of Pt/C and Pt/OMC with pristine Pt nanoparticle electrocatalysts, conversion of glycerol to GLA was the dominant reaction at all times (Fig. 5c-e and Table S8). After 1 and 3 h, the GLA selectivity of Pt/C was 54.5% and 63.5%, respectively. The Pt/OMC exhibited GLA selectivity of 54.1% and 58.8% after 1 and 3 h, respectively (Fig. 5e). In contrast, the DHA selectivity of Pt/C and Pt/OMC was only 7.2% and 11.3%, respectively after 1 h (Fig. 5f). It confirmed that the use of OMC as support material is a promising way to improve the overall reaction rate and glycerol conversion during the EGOR process, but that it is not an effective way to modulate the reaction pathway and increase the DHA selectivity. On the other hand, $SbO_x$-Pt/OMC electrocatalysts showed significantly enhanced DHA selectivity compared with Pt/C and Pt/OMC. After 1 h, DHA selectivity of $SbO_x$-Pt/OMC-1, $SbO_x$-Pt/OMC-2, and $SbO_x$-Pt/OMC-3 was 60.1%, 81.1%, and 53.2%, respectively, implying that the enhanced DHA selectivity originated from the incorporation of amorphous $SbO_x$ on the Pt surface and could modulate the reaction pathway of EGOR. After 3 h, $SbO_x$-Pt/OMC electrocatalysts still showed high DHA selectivity. Most importantly, $SbO_x$-Pt/OMC-2 had the highest DHA selectivity among three $SbO_x$-Pt/OMC electrocatalysts after 1 and 3 h of the EGOR process, manifesting that moderate control of the amount of amorphous $SbO_x$ on the Pt surface is crucial to maximizing the DHA selectivity. It is noteworthy that the DHA selectivity of 81.1% achieved by $SbO_x$-Pt/OMC-2 was significantly higher compared to other electrocatalysts previously reported (Table S9). Furthermore, long-term stability of $SbO_x$-Pt/OMC-2 was also investigated by CA techniques for 120 h (Fig. 5g, h, and Table S10). In the case of Pt/C electrocatalyst, DHA selectivity was only 7.2% after 120 h (Fig. 5g). Further, Pt/C exhibited low glycerol conversion (20.8%) and reaction rate (1.47 $mmol_{Gly}$ $mol_{Pt}^{-1}$ $h^{-1}$) after 120 h. On the other hand, $SbO_x$-Pt/OMC-2 showed much higher DHA selectivity of 53.1% (~7.4 times higher) than Pt/C even after 120 h (Fig. 5h). The glycerol conversion and reaction rate of $SbO_x$-Pt/OMC-2 after 120 h were 32.2% and 2.73 $mmol_{Gly}$ $mol_{Pt}^{-1}$ $h^{-1}$, respectively, higher than those of Pt/C. It is also noteworthy that DHA selectivity of $SbO_x$-Pt/OMC-2 was well-maintained at high value ($> 50\%$) during the long-term stability test. Consequently, we believe that the strategy of depositing amorphous

$SbO_x$ on the surface of Pt particles is a promising way to increase the DHA selectivity, glycerol conversion, and reaction rate of the EGOR process. Moreover, ICP-MS analysis of electrolyte was also performed to investigate the stability of Pt active site for glycerol oxidation in acidic condition (Table S11). After long-term CA test for 120 h, Pt/C showed 10.59 μg of Pt in electrolyte (*i.e.,* loss of 1.38% of Pt in Pt/C). On the other hand, it is noteworthy that $SbO_x$-Pt/OMC-2 showed only $< 0.50$ μg of Pt in electrolyte (*i.e.,* loss of $< 0.08\%$ of Pt in $SbO_x$-Pt/OMC-2) even after 120 h, that is ~21 times lower dissolution ratio than that of Pt/C. It indicates that incorporation of $SbO_x$ on Pt surface effectively inhibits the dissolution of Pt into the acidic electrolyte, hence Pt active site for glycerol oxidation can be well-retained. However, ICP-MS results of $SbO_x$-Pt/OMC-2 showed that $SbO_x$ was also leached out to some extent after long-term EGOR, which is the reason why conversion and reaction rate decreased gradually in $SbO_x$-Pt/OMC-2 electrocatalysts.

## 3.4. Origin of high DHA selectivity with $SbO_x$-Pt electrocatalyst

The proposed series of material characterizations and electrochemical analyses suggest that the DHA selectivity of Pt electrocatalysts can be significantly improved by the incorporation of amorphous $SbO_x$ on the Pt surface. To unveil the origin of this different DHA selectivity by amorphous $SbO_x$, we performed a DFT calculation. In the reaction pathway in EGOR (Fig. S22), glycerol was first oxidized to GAD and DHA, and further oxidation of DHA, GAD, GLA to GCA, HPA, TTA, oxalic acid (OXA), and formic acid (FA) can occur in EGOR [25]. In our work, glycerol was oxidized to GLA mainly on Pt-based electrocatalysts. On the other hand, when $SbO_x$ was present in the Pt-based electrocatalyst, a secondary alcohol oxidation reaction of glycerol occurred, and DHA selectivity increased. Thus, the DFT calculations were performed to further verify the glycerol oxidation on the Pt surface with and without $SbO_x$. The cubic senarmontite $Sb_2O_3$-based $Sb_4O_6$ cluster structure was used to simulate a small amount of $SbO_x$ as illustrated in Fig. S23 [47]. In the case of glycerol adsorption, it was more strongly adsorbed when $Sb_4O_6$ was present on the Pt (111) surface ($\Delta E_{ad}$ (gly, Pt-$Sb_4O_6$) $= -0.516$ eV) than when only Pt was used ($\Delta E_{ad}$ (gly, Pt) $= -0.283$ eV) (Fig. S23). The difference in the interaction between glycerol and an electrocatalyst greatly influenced the reaction path [23]. The GAD and DHA formation processes were calculated in the existence of applied potential of 0.920 V (almost same with experimental condition) to identify the preferred reaction pathways in Pt and $SbO_x$-Pt (Fig. 6a, b, and Table S12). In the case of Pt, the formation of DHA was slightly more stable (0.086 eV) than in the case of GAD, but considering the intermediate path, there was a high possibility that GAD would be generated. In Pt with a $Sb_4O_6$ cluster, DHA formation was much more thermodynamically stable by 0.454 eV than GAD formation. In addition, even when looking at the intermediate path (Step1, Fig. 6b), the DHA formation process was energetically stable at the $SbO_x$-Pt. This data was consistent with the experimental results in which $SbO_x$ increased DHA selectivity, and it was expected that Sb affected the reaction pathway. To demonstrate electron distribution and binding characteristics of Sb, a charge density difference and Bader charge analysis was performed [48]. As shown in Fig. 6c and d, electrons were reduced by $-2.070e$ in Sb and increased by $+1.221e$ and $+1.064e$ in oxygen of DHA, forming a strong ionic bond. Conversely, $Sb_4O_6$ showed a weak chemical interaction with GAD. This electron transfer that derived a strong ionic bond was not observed on the surface of bare Pt (Fig. 6e and f). It can be observed that the calculated electron localization function (ELF) results also show that the oxygen of DHA and the Sb of the electrocatalyst exhibit electron distributions corresponding to ionic bonding (Fig. S24). A strong interaction between DHA and $Sb_4O_6$-Pt can inhibit the formation of GAD and further oxidation, and thereby improved DHA selectivity. In the case of Pt, further oxidation occurred in GAD to form GLA, which was thermodynamically very stable. However, in the presence of $SbO_x$, the activation barrier of the intermediate state (Step 3) for GLA formation was very large because the repulsive force between the
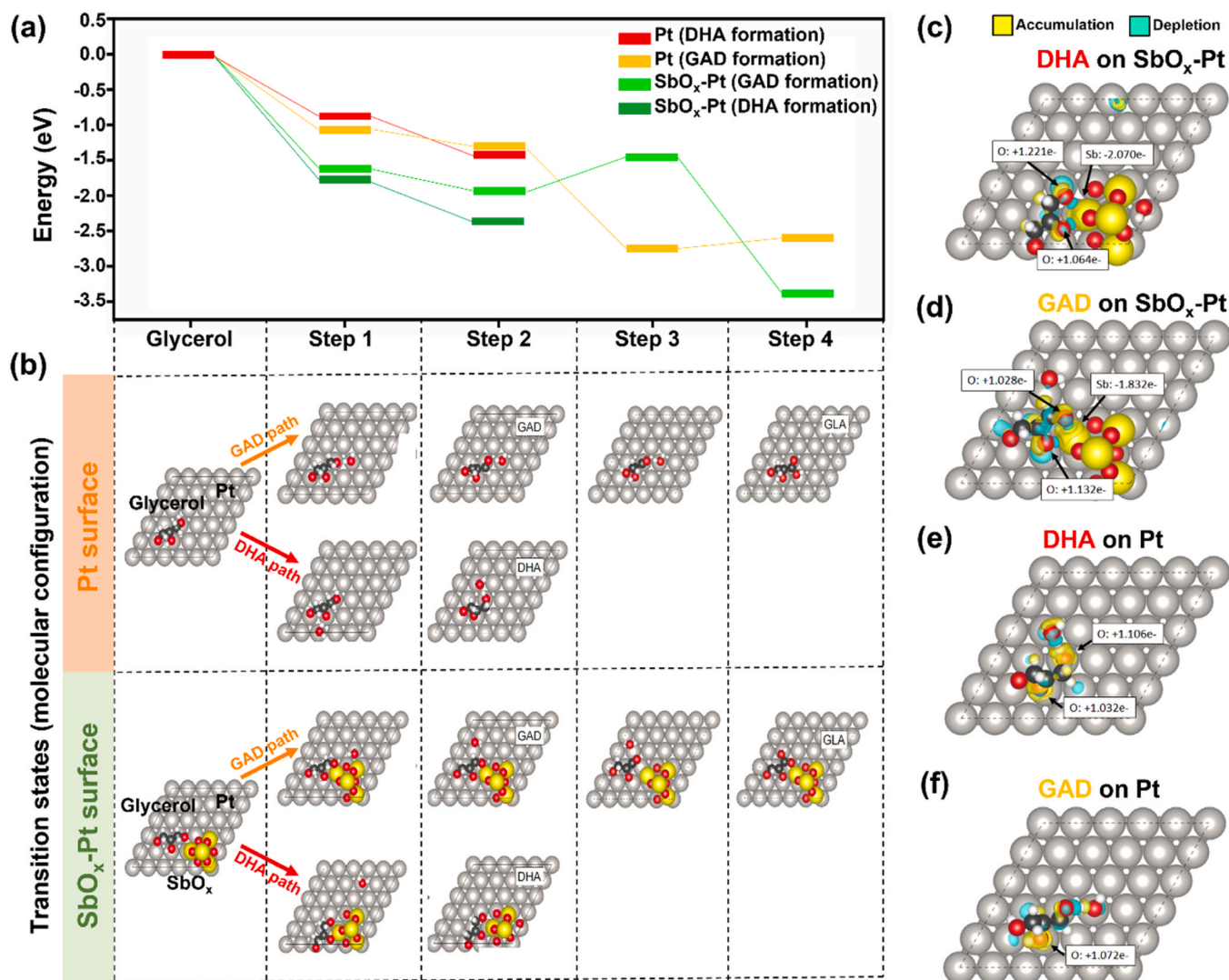
**Fig. 6.** (a) Free energy diagram of GAD and DHA formation on Pt and SbO$_x$-Pt electrocatalysts. (b) Molecular configuration for transition state of each pathway. Top view of the calculated charge density difference of (c) DHA* and (d) GAD* on Pt-Sb$_4$O$_6$ and (e) DHA* and (f) GAD* on a Pt surface (Isosurface level: 0.002 e/Bohr$^3$). Silver, red, dark gray, white, and yellow balls represent Pt, O, C, H, and Sb, respectively.

oxygen in the SbO$_x$ and the oxygen in the intermediate state became strong, and the adsorption energy became weak. Therefore, when there was only Pt, GLA mainly formed, and DHA selectivity increased when SbO$_x$ was present. As the size of the SbO$_x$ cluster increased, a Sb$_2$O$_3$ phase transition occurred [49], and the Sb exposed to the surface decreased, and the site that induced DHA production disappeared. Therefore, the influence of Pt increased, and GAD formation became easier, and was similar to the product selectivity of Pt/C and Pt/OMC. In the final step, DHA is readily detached due to the solvation effect of water [50].

## 4. Conclusion

In summary, we reported the synergistic effect of a porous carbon support with cylindrical mesopores and an amorphous SbO$_x$ incorporated Pt nanoparticle electrocatalyst to simultaneously achieve extraordinary DHA selectivity, high activity, and stability of the EGOR in an acidic condition. The mesoporous carbon with a high surface area increased the reaction activity and rate for the glycerol oxidation reaction and also inhibited the aggregation of Pt electrocatalysts during cycling. Furthermore, deposition of amorphous SbO$_x$ on the surface of Pt nanoparticles modulated the intermediates adsorption energy on the Pt

electrocatalysts, which changed the glycerol oxidation pathway. In this process, in particular, Sb atom in SbO$_x$ donates electrons to O atom of DHA, which results in the formation of strong binding with DHA, whereas the GAD adsorption on SbO$_x$ is weak. This selectively strong adsorption of DHA on the surface of SbO$_x$ deposited Pt electrocatalysts allows the glycerol to be selectively oxidized to DHA. Consequently, this specially designed electrocatalyst has 11.2 times higher DHA selectivity than Pt/C and achieves a significantly high DHA selectivity of 81.1% for the EGOR process with outstanding cycle stability up to 1000 cycles. We believe that this strategy to selectively modulate the adsorption configuration and strength of EGOR products by deposition of amorphous SbO$_x$ on the Pt surface creates a promising avenue for the design of advanced electrocatalysts for glycerol oxidation.

## CRediT authorship contribution statement

**Dongkyu Kim:** Conceptualization, Methodology, Validation, Formal analysis, Investigation, Data curation, Writing – original draft, Writing – review & editing, Visualization. **Won-Gwang Lim:** Conceptualization, Methodology, Validation, Formal analysis, Investigation, Data curation, Writing – original draft, Writing – review & editing, Visualization. **D. Kim, W.-G. Lim:** Contributed equally to this work.

**Youngmin Kim:** Validation, Formal analysis, Investigation, Data curation. **Lee Seul Oh:** Validation, Formal analysis, Investigation, Data curation. **Seongseop Kim:** Validation, Discussion, Investigation, Data curation. **Jong Hyeok Park:** Validation, Formal analysis, Investigation, Data curation. **Changshin Jo:** Discussion, Investigation, Data curation. **Hyung Ju Kim:** Funding acquisition, Discussion, Investigation, Data curation. **Joonhee Kang:** Software, Resources, Supervision, Funding acquisition, Validation, Formal analysis, Investigation, Data curation, Writing – review & editing, Visualization. **Seonggyu Lee:** Conceptualization, Methodology, Resources, Supervision, Validation, Formal analysis, Investigation, Data curation, Writing – review & editing, Visualization. **Eunho Lim:** Conceptualization, Methodology, Resources, Supervision, Funding acquisition, Validation, Formal analysis, Investigation, Data curation, Writing – review & editing, Visualization, Project administration.

## Declaration of Competing Interest

The authors declare that they have no known competing financial interests or personal relationships that could have appeared to influence the work reported in this paper.

## Data availability

Data will be made available on request.

## Acknowledgement

## Appendix A. Supporting information

Supplementary data associated with this article can be found in the online version at doi:10.1016/j.apcatb.2023.123104.

## References

[1] M.R. Monteiro, C.L. Kugelmeier, R.S. Pinheiro, M.O. Batalha, A. da Silva César, Glycerol from biodiesel production: Technological paths for sustainability, Renew. Sustain. Energy Rev. 88 (2018) 109–122.

[2] L. Fan, B. Liu, X. Liu, N. Senthilkumar, G. Wang, Z. Wen, Recent progress in electrocatalytic glycerol oxidation, Energy Technol. 9 (2021) 2000804.

[3] A.L.C. Minh, S.P. Samudrala, S. Bhattacharya, Valorisation of glycerol through catalytic hydrogenolysis routes for sustainable production of value-added C3 chemicals: current and future trends, Sustain. Energy Fuels 6 (2022) 596–639.

[4] M. Anitha, S. Kamarudin, N. Kofli, The potential of glycerol as a value-added commodity, Chem. Eng. J. 295 (2016) 119–130.

[5] J. McNutt, J. Yang, Utilization of the residual glycerol from biodiesel production for renewable energy generation, Renew. Sustain. Energy Rev. 71 (2017) 63–76.

[6] N. Gupta, O. Khavryuchenko, A. Villa, D. Su, Metal-Free Oxidation of Glycerol over Nitrogen-Containing Carbon Nanotubes, ChemSusChem 10 (2017) 3030–3034.

[7] A.C. Garcia, M.J. Kolb, C. van Nierop y Sanchez, J. Vos, Y.Y. Birdja, Y. Kwon, G. Tremiliosi-Filho, M.T. Koper, Strong impact of platinum surface structure on primary and secondary alcohol oxidation during electro-oxidation of glycerol, ACS Catal. 6 (2016) 4491–4500.

[8] H.J. Kim, Y. Kim, D. Lee, J.-R. Kim, H.-J. Chae, S.-Y. Jeong, B.-S. Kim, J. Lee, G. W. Huber, J. Byun, Coproducing value-added chemicals and hydrogen with electrocatalytic glycerol oxidation technology: experimental and techno-economic investigations, ACS Sustain. Chem. Eng. 5 (2017) 6626–6634.

[9] Z. He, J. Hwang, Z. Gong, M. Zhou, N. Zhang, X. Kang, J.W. Han, Y. Chen, Promoting biomass electrooxidation via modulating proton and oxygen anion deintercalation in hydroxide, Nat. Commun. 13 (2022) 3777.

[10] M.K. Goetz, M.T. Bender, K.-S. Choi, Predictive control of selective secondary alcohol oxidation of glycerol on NiOOH, Nat. Commun. 13 (2022) 5848.

[11] X. Yu, E.C. Dos Santos, J. White, G. Salazar-Alvarez, L.G. Pettersson, A. Cornell, M. Johnsson, Electrocatalytic glycerol oxidation with concurrent hydrogen evolution utilizing an efficient $MoO_x$/Pt catalyst, Small 17 (2021) 2104288.

[12] Y. Zhou, Y. Shen, J. Xi, X. Luo, Selective electro-oxidation of glycerol to dihydroxyacetone by PtAg skeletons, ACS Appl. Mater. Interfaces 11 (2019) 28953–28959.

[13] Y. Pei, Z. Pi, H. Zhong, J. Cheng, F. Jin, Glycerol oxidation-assisted electrochemical $CO_2$ reduction for the dual production of formate, J. Mater. Chem. A 10 (2022) 1309–1319.

[14] M. Li, T. Wang, W. Zhao, S. Wang, Y. Zou, A pair-electrosynthesis for formate at ultra-low voltage via coupling of $CO_2$ reduction and formaldehyde oxidation, Nano-Micro Lett. 14 (2022) 211.

[15] K. Fernández-Caso, A. Pena-Rodríguez, J. Solla-Gullón, V. Montiel, G. Díaz-Sainz, M. Alvarez-Guerra, A. Irabien, Continuous carbon dioxide electroreduction to formate coupled with the single-pass glycerol oxidation to high value-added products, J. $CO_2$ Util. 70 (2023), 102431.

[16] L.S. Oh, M. Park, Y.S. Park, Y. Kim, W. Yoon, J. Hwang, E. Lim, J.H. Park, S. M. Choi, M.H. Seo, How to change the reaction chemistry on nonprecious metal oxide nanostructure materials for electrocatalytic oxidation of biomass-derived glycerol to renewable chemicals, Adv. Mater. (2022) 2203285.

[17] D. Lee, Y. Kim, H. Han, W.B. Kim, H. Chang, T.-M. Chung, J.H. Han, H.W. Kim, H. J. Kim, Atomic-layer-deposited $SnO_2$ on Pt/C prevents sintering of Pt nanoparticles and affects the reaction chemistry for the electrocatalytic glycerol oxidation reaction, J. Mater. Chem. A 8 (2020) 15992–16005.

[18] T.-G. Vo, P.-Y. Ho, C.-Y. Chiang, Operando mechanistic studies of selective oxidation of glycerol to dihydroxyacetone over amorphous cobalt oxide, Appl. Catal. B: Environ. 300 (2022), 120723.

[19] H. Sheng, A.N. Janes, R.D. Ross, H. Hofstetter, K. Lee, J. Schmidt, S. Jin, Linear paired electrochemical valorization of glycerol enabled by the electro-Fenton process using a stable $NiSe_2$ cathode, Nat. Catal. 5 (2022) 716–725.

[20] D. Kim, L.S. Oh, Y.C. Tan, H. Song, H.J. Kim, J. Oh, Enhancing glycerol conversion and selectivity toward glycolic acid via precise nanostructuring of electrocatalysts, ACS Catal. 11 (2021) 14926–14931.

[21] D. Lee, Y. Kim, Y. Kwon, J. Lee, T.-W. Kim, Y. Noh, W.B. Kim, M.H. Seo, K. Kim, H. J. Kim, Boosting the electrocatalytic glycerol oxidation performance with highly-dispersed Pt nanoclusters loaded on 3D graphene-like microporous carbon, Appl. Catal. B: Environ. 245 (2019) 555–568.

[22] S. Lee, H.J. Kim, E.J. Lim, Y. Kim, Y. Noh, G.W. Huber, W.B. Kim, Highly selective transformation of glycerol to dihydroxyacetone without using oxidants by a PtSb/C-catalyzed electrooxidation process, Green. Chem. 18 (2016) 2877–2887.

[23] Y. Kim, H.W. Kim, S. Lee, J. Han, D. Lee, J.R. Kim, T.W. Kim, C.U. Kim, S.Y. Jeong, H.J. Chae, The role of ruthenium on carbon-supported PtRu catalysts for electrocatalytic glycerol oxidation under acidic conditions, ChemCatChem 9 (2017) 1683–1690.

[24] Y. Kwon, Y. Birdja, I. Spanos, P. Rodriguez, M.T. Koper, Highly selective electro-oxidation of glycerol to dihydroxyacetone on platinum in the presence of bismuth, ACS Catal. 2 (2012) 759–764.

[25] C. Liu, M. Hirohara, T. Maekawa, R. Chang, T. Hayashi, C.-Y. Chiang, Selective electro-oxidation of glycerol to dihydroxyacetone by a non-precious electrocatalyst–CuO, Appl. Catal. B: Environ. 265 (2020), 118543.

[26] C. Dai, L. Sun, H. Liao, B. Khezri, R.D. Webster, A.C. Fisher, Z.J. Xu, Electrochemical production of lactic acid from glycerol oxidation catalyzed by AuPt nanoparticles, J. Catal. 356 (2017) 14–21.

[27] B. Katryniok, H. Kimura, E. Skrzyńska, J.-S. Girardon, P. Fongarland, M. Capron, R. Ducoulombier, N. Mimura, S. Paul, F. Dumeignil, Selective catalytic oxidation of glycerol: perspectives for high value chemicals, Green. Chem. 13 (2011) 1960–1979.

[28] Y. Wang, L. Li, L. Hu, L. Zhuang, J. Lu, B. Xu, A feasibility analysis for alkaline membrane direct methanol fuel cell: thermodynamic disadvantages versus kinetic advantages, Electrochem. Commun. 5 (2003) 662–666.

[29] Y. Meng, D. Gu, F. Zhang, Y. Shi, H. Yang, Z. Li, C. Yu, B. Tu, D. Zhao, Ordered mesoporous polymers and homologous carbon frameworks: amphiphilic surfactant templating and direct transformation, Angew. Chem. Int. Ed. 44 (2005) 7053–7059.

[30] J. Shim, J. Lee, Y. Ye, J. Hwang, S.-K. Kim, T.-H. Lim, U. Wiesner, J. Lee, One-pot synthesis of intermetallic electrocatalysts in ordered, large-pore mesoporous carbon/silica toward formic acid oxidation, ACS Nano 6 (2012) 6870–6881.

[31] J. Han, Y. Kim, D.H. Jackson, H. Chang, H.W. Kim, J. Lee, J.-R. Kim, Y. Noh, W. B. Kim, K.-Y. Lee, Enhanced catalytic performance and changed reaction chemistry for electrochemical glycerol oxidation by atomic-layer-deposited Pt-nanoparticle catalysts, Appl. Catal. B: Environ. 273 (2020), 119037.

[32] N.G. Akalework, C.-J. Pan, W.-N. Su, J. Rick, M.-C. Tsai, J.-F. Lee, J.-M. Lin, L.-D. Tsai, B.-J. Hwang, Ultrathin $TiO_2$-coated MWCNTs with excellent conductivity and SMSI nature as Pt catalyst support for oxygen reduction reaction in PEMFCs, J. Mater. Chem. 22 (2012) 20977–20985.

[33] X. Xie, Y. Nie, S. Chen, W. Ding, X. Qi, L. Li, Z. Wei, A catalyst superior to carbon-supported-platinum for promotion of the oxygen reduction reaction: reduced-polyoxometalate supported palladium, J. Mater. Chem. A 3 (2015) 13962–13969.

[34] G. Kresse, J. Furthmüller, Efficient iterative schemes for ab initio total-energy calculations using a plane-wave basis set, Phys. Rev. B 54 (1996) 11169.

[35] J.P. Perdew, K. Burke, M. Ernzerhof, Generalized gradient approximation made simple, Phys. Rev. Lett. 77 (1996) 3865.

[36] P.E. Blöchl, Projector augmented-wave method, Phys. Rev. B 50 (1994) 17953.

[37] J. Lee, M. Christopher Orilall, S.C. Warren, M. Kamperman, F.J. Disalvo, U. Wiesner, Direct access to thermally stable and highly crystalline mesoporous transition-metal oxides with uniform pores, Nat. Mater. 7 (2008) 222–228.

[38] Ad Pozio, M. De Francesco, A. Cemmi, F. Cardellini, L. Giorgi, Comparison of high surface Pt/C catalysts by cyclic voltammetry, J. Power Sources 105 (2002) 13–19.

[39] S. Mukerjee, S. Srinivasan, M.P. Soriaga, J. McBreen, Effect of preparation conditions of Pt alloys on their electronic, structural, and electrocatalytic activities for oxygen reduction-XRD, XAS, and electrochemical studies, J. Phys. Chem. 99 (1995) 4577–4589.

[40] S.C. Kim, C.Y. Park, The complete oxidation of a volatile organic compound (toluene) over supported metal oxide catalysts, Res. Chem. Intermed. 28 (2002) 441–449.

[41] X. Yu, P.G. Pickup, Codeposited PtSb/C catalysts for direct formic acid fuel cells, J. Power Sources 196 (2011) 7951–7956.

[42] F. Garbassi, XPS and AES study of antimony oxides, Surf. Interface Anal. 2 (1980) 165–169.

[43] N. Karikalan, M. Elavarasan, T.C. Yang, Studies on the sonochemical polymorphism of $Sb_2O_3$ on activated graphite for the electrochemical determination of imipramine, Ultrason. Sonochem. 64 (2020), 105012.

[44] J. Fei, Y. Cui, J. Li, Z. Xu, J. Yang, R. Wang, Y. Cheng, J. Hang, A flexible $Sb_2O_3$/ carbon cloth composite as a free-standing high performance anode for sodium ion batteries, Chem. Commun. 53 (2017) 13165–13167.

[45] F. Ando, T. Gunji, T. Tanabe, I. Fukano, H.D. Abruna, J. Wu, T. Ohsaka, F. Matsumoto, Enhancement of the Oxygen Reduction Reaction Activity of Pt by Tuning Its d-Band Center via Transition Metal Oxide Support Interactions, ACS Catal. 11 (2021) 9317–9332.

[46] I. Jiménez-Morales, S. Cavaliere, D. Jones, J. Rozière, Strong metal–support interaction improves activity and stability of Pt electrocatalysts on doped metal oxides, Phys. Chem. Chem. Phys. 20 (2018) 8765–8772.

[47] B. Kaiser, T.M. Bernhardt, M. Kinne, K. Rademann, A. Heidenreich, Formation, stability, and structures of antimony oxide cluster ions, J. Chem. Phys. 110 (1999) 1437–1449.

[48] G. Henkelman, A. Arnaldsson, H. Jónsson, A fast and robust algorithm for Bader decomposition of charge density, Comput. Mater. Sci. 36 (2006) 354–360.

[49] W. Han, P. Huang, L. Li, F. Wang, P. Luo, K. Liu, X. Zhou, H. Li, X. Zhang, Y. Cui, Two-dimensional inorganic molecular crystals, Nat. Commun. 10 (2019) 1–10.

[50] N. Shan, B. Liu, Elucidating molecular interactions in glycerol adsorption at the metal–water interface with density functional theory, Langmuir 35 (2018) 4791–4805.